
This manuscript has been submitted for publication in EARTH AND PLANETARY SCIENCE LETTERS. Please note that this manuscript has not undergone peer review, nor has it been formally accepted for publication. Subsequent versions of this manuscript may have slightly different content. If accepted, the final version of this manuscript will be available via the 'Peer-reviewed Publication DOI' link on the right-hand side of this webpage. Please feel free to contact the corresponding author; we welcome feedback.

Supplementary information for:

Primordial and recycled sulfur sampled by the Iceland mantle plume

Eemu Ranta^{1*}, Jóhann Gunnarsson-Robin¹, Sæmundur A. Halldórsson¹, Shuhei Ono², Gareth Izon², Matthew G. Jackson³, Callum D.J. Reekie⁴, Frances E. Jenner⁵, Guðmundur H. Guðfinnsson¹, Ólafur P. Jónsson¹, Andri Stefánsson¹

¹*Nordic Volcanological Center, Institute of Earth Sciences, University of Iceland, Iceland*

²*Department of Earth, Atmospheric and Planetary Sciences, Massachusetts Institute of Technology, USA*

³*Department of Earth Science, University of California, Santa Barbara, USA*

⁴*Department of Earth Sciences, University of Cambridge, UK*

⁵*School of Environment, Earth and Ecosystem Sciences, The Open University, UK*

*Corresponding author: Eemu Ranta, eemu@hi.is

The supplementary material includes:

1. Analytical details
2. Evaluation of magmatic S degassing
3. Model I: Quantitative model of sulfide melt formation
4. Bulk $\delta^{34}\text{S}$ values of Iceland samples
5. Model II: $\delta^{34}\text{S}$ fractionation during degassing
6. Relationship between melt $\text{S}^{6+}/\Sigma\text{S}$ and f_{O_2}
7. Model III: Effect of sulfide fractionation on $\delta^{34}\text{S}$

Figures S1-S7

Table S1: Replicate S isotope analyses of standards

Table S2: Replicate S isotope analyses of basaltic glasses

Table S3: Compilation of $\Delta^{33}\text{S}_{\text{CDT}}$ and $\Delta^{36}\text{S}_{\text{CDT}}$ definitions

Table S4: Main data table

Table S5: Supporting data table

Table S6: Mantle end-member compositions

1. Analytical details

1.1 Electron probe microanalysis (EPMA)

Major element and S concentrations in glasses were determined by electron probe microanalysis (EPMA) using the JEOL JXA-8230 SuperProbe at the Institute of Earth Sciences, University of Iceland, following the protocol outlined in Bali et al. (2018). In brief, sulfur concentrations were determined by wavelength-dispersive spectrometry (WDS), using a 10-15 μm diameter beam and peak/background counting times of 100s. Reported concentrations represent averages computed from 6-11 spot analyses, with typical 1σ errors of $\pm 5\%$. To determine S speciation ($\text{S}^{6+}/\Sigma\text{S}$, where $\Sigma\text{S} = \text{S}^{6+} + \text{S}^{2-}$), $\Delta\lambda\text{S}_{\text{K}\alpha}$ peak shifts were measured by EPMA following the method of Carrol and Rutherford (1988). Peak positions of $\text{S}^{6+}_{\text{K}\alpha}$ and $\text{S}^{2-}_{\text{K}\alpha}$ were calibrated with in-house pyrite and anhydrite standards. Each $\text{S}^{6+}/\Sigma\text{S}$ datapoint constitutes an average of three analyses with typical 1σ errors of ± 0.05 .

1.2 Inductively coupled plasma mass spectrometry (ICP-MS)

Trace element concentrations were determined from dissolved glass powders by inductively coupled plasma mass spectrometry (ICP-MS) at the Scripps Institution of Oceanography using a Thermo-Fischer Element-2 ICP-MS following the method described in Halldórsson et al. (2016a). Copper concentrations were determined by laser ablation ICP-MS (LA-ICP-MS) at the Research School of Earth Sciences, Australian National University, following the methods of Jenner and O'Neill (2012), for all samples with the exception of the KVK-2xx series. Trace elements (including Cu) for the KVK-2xx samples were analyzed at the Geological Survey of Finland, Espoo, by LA-ICP-MS using a Nu AttoM instrument. The analytical protocol used was similar to the one outlined in Moilanen et al. (2020), except BCR-2G was used as a calibrating standard. Reported values are based on the average of 6-11 point analyses. Trace element data for the KVK-2xx glasses were reduced using the SILLS software package (Guillong et al. 2008).

1.3 Accuracy and precision of S isotope measurements

We estimate the long-term reproducibility of our $\delta^{34}\text{S}$, $\Delta^{33}\text{S}$ and $\Delta^{36}\text{S}$ measurements via replicate measurements of IAEA-S-1 Ag_2S standard and an in-house Ag_2S standard (Ono-

Ag₂S, Sigma Aldrich), fluorinated and measured alongside our samples during 7 measurement sessions that span four years (2016-2020). The long-term average $\delta^{34}\text{S}$, $\Delta^{33}\text{S}$ and $\Delta^{36}\text{S}$ values of IAEA-S-1 relative to our laboratory reference gas (SG1) were -1.19 ± 0.17 ‰, 0.100 ± 0.004 ‰ and -0.669 ± 0.028 ‰, respectively (1σ , $n = 10$). The $\delta^{34}\text{S}_{\text{S-1/SG1}}$ value of IAEA-S-1 is used to convert measured isotope ratios to V-CDT notation using the certified value for IAEA-S-1 of $\delta^{34}\text{S}_{\text{S-1/V-CDT}} = -0.3$ ‰ (Coplen and Krouse 1998). The long-term average values for $\delta^{34}\text{S}$, $\Delta^{33}\text{S}$ and $\Delta^{36}\text{S}$ of our lab Ag₂S standard relative to SG1 are 0.97 ± 0.12 ‰, 0.020 ± 0.004 ‰ and -0.029 ± 0.086 ‰, respectively (1σ , $n = 18$; Fig. S1). The reproducibilities of these standards are similar, reflecting the uncertainty associated with fluorination and mass spectrometry. Given the higher number of analyses, we conservatively adopt the standard deviation calculated from replicate analyses of Ono-Ag₂S as the estimate of our long-term reproducibility for $\delta^{34}\text{S}$, $\Delta^{33}\text{S}$ and $\Delta^{36}\text{S}$.

To estimate errors related to S extraction and glass heterogeneity, two Icelandic subglacial glasses STAP-1 ($n = 11$) and A35 ($n = 6$) were repeatedly extracted and measured (Fig. S1; Table S2). Compared with the Ag₂S standards, replicate analyses of these sample standards returned larger standard deviations (Fig. S1). The source of the larger 1σ uncertainty suggests either minor intra-sample S isotopic heterogeneity, or an additional uncertainty related to the extraction process. Individual extractions of the glasses produced variable yields (57–105 %). Low yields may have resulted from incomplete extractions, lower-than-expected S²⁻ concentration in the dissolved sample (because of high crystal content or high S⁶⁺/ΣS), or weighing error. Experimental processing of known quantities of sulfide limits mechanical Ag₂S losses to less than 8%. While incomplete extractions could yield artificially high measured $\delta^{34}\text{S}$ values because of the positive fractionation factor associated with the conversion of dissolved S²⁻ to H₂S gas at 300 °C ($1000 \ln a_{\text{H}_2\text{S}-\text{S}^{2-}} \approx 3$ ‰; Supplementary Information section 5), the lack of correlation between yields and isotopic composition (Fig. S1) renders this unlikely. Consequently, we consider the variable yields to reflect variable glass/crystal content of the extracted material and thus we conclude that the larger isotopic variability associated with measurements of STAP-1 and A35 likely reflects isotopic heterogeneity present in the subglacial glasses.

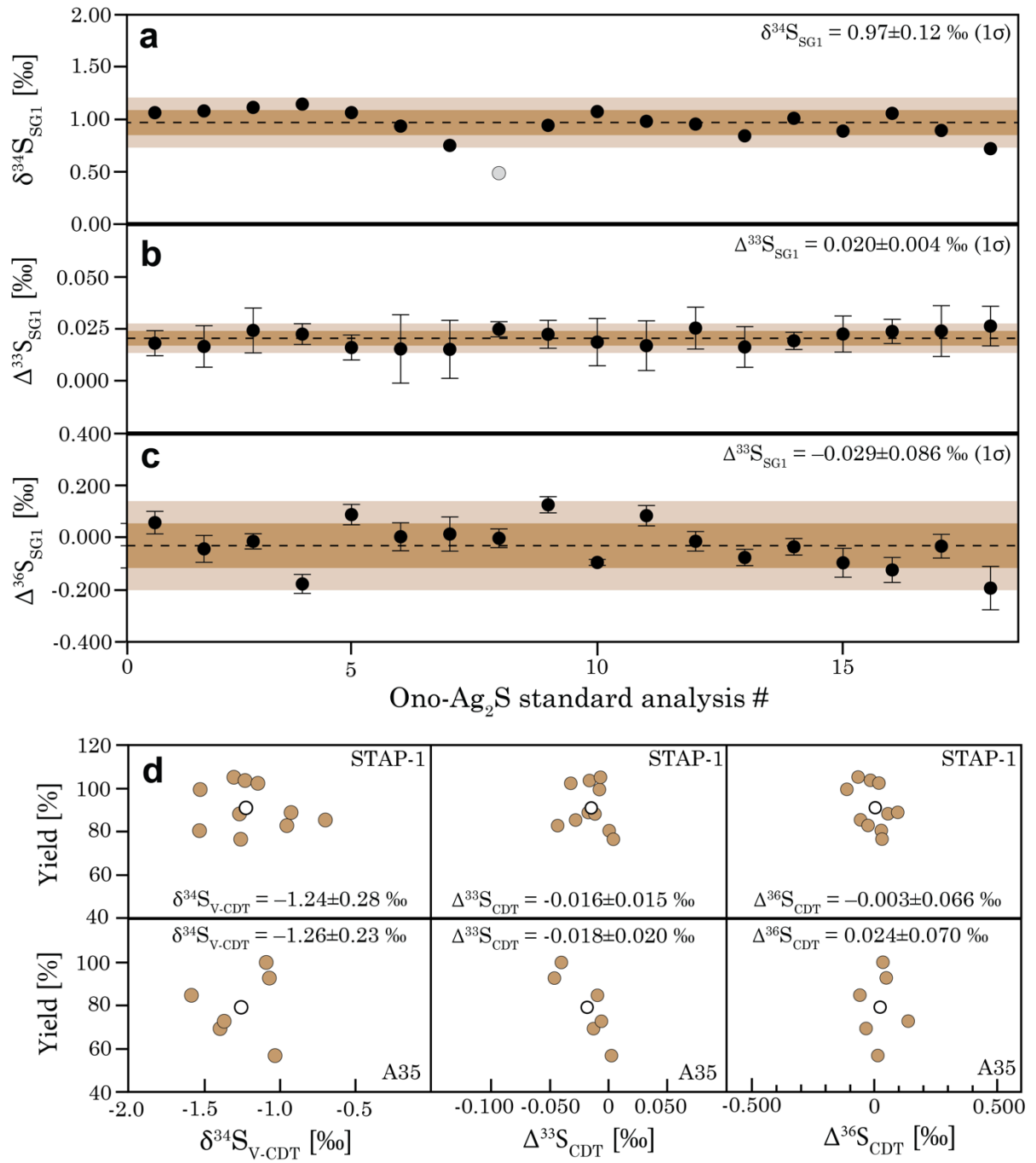


Figure S1 (a)-(c) Evaluation of analytical uncertainty associated with S isotope measurements. Data is shown for the Ono- Ag_2S standard ($n = 18$), which was analyzed during all 7 sessions. Shaded show respective 1 and 2σ of the average. Error bars indicate 2 standard errors based on 6 measurement cycles. For $\delta^{34}\text{S}$, the instrumental error is smaller than the size of the symbols. One measurement (grey circle) is excluded from the $\delta^{34}\text{S}$ average, as it falls outside 3σ uncertainty. **(d)** Replicate standard glass analyses for STAP-1 and A35 show that measured S isotope compositions do not correlate with yields. Data is reported in Tables S1 and S2.

1.4 Definition of the $\Delta^{33}\text{S}$ and $\Delta^{36}\text{S}$ scales relative to CDT

Given the small $\Delta^{33}\text{S}$ variability in basaltic glasses, a well-defined reference scale is paramount to make comparisons between $\Delta^{33}\text{S}$ datasets produced at different laboratories. While IAEA-S-1 is the certified reference material that anchors $\delta^{34}\text{S}$ to the V-CDT-scale (Coplen and Krouse, 1998), as yet, it lacks certified values for $\delta^{33}\text{S}$ and $\delta^{36}\text{S}$. Consequently, $\Delta^{33}\text{S}$ and $\Delta^{36}\text{S}$ values are either reported relative to a laboratory reference gas (e.g. Labidi et al. 2012), which conceivably has different S isotopic compositions at different labs, or are anchored to the CDT-scale via coupled measurements of IAEA-S-1 and CDT (Ono et al. 2006, Labidi et al. 2016, Antonelli et al. 2014).

We compiled coupled IAEA-S-1 and CDT measurements that have been used to anchor the former to the $\Delta^{33}\text{S}_{\text{CDT}}$ scale in studies conducted at the University of Maryland (Antonelli et al. 2014, Labidi et al. 2017), the Geophysical Laboratory, Carnegie Institute of Washington (Ono et al. 2006, Ono et al. 2007) and the Laboratoire de Géochimie des Isotopes Stables, Institut de Physique du Globe de Paris (Labidi et al. 2012, Labidi et al., 2014, Defouilloy et al. 2016) and calculated the associated standard deviations (Table S-3, Fig. S-2). In these studies, the definitions of the $\Delta^{33}\text{S}_{\text{CDT}}$ scale vary from IAEA-S-1 values of $\Delta^{33}\text{S}_{\text{CDT}} = 0.093 \pm 0.013 \text{ ‰}$ (GL: Ono et al. 2007; based on 3 laser fluorinations of CDT) to $\Delta^{33}\text{S}_{\text{CDT}} = 0.118 \pm 0.006 \text{ ‰}$ (UMD: Labidi et al. 2017). It is not known with certainty whether the slight differences reflect analytical differences between laboratories or heterogeneities within CDT itself.

The average IAEA-S-1 definitions based on 8 studies are $\Delta^{33}\text{S}_{\text{CDT}} = 0.109 \pm 0.006 \text{ ‰}$ and $\Delta^{36}\text{S}_{\text{CDT}} = -0.730 \pm 0.153 \text{ ‰}$ (both errors reflect 95% confidence intervals; Fig. S2). As CDT has not been measured at the MIT, we use these average definitions of $\Delta^{33}\text{S}_{\text{CDT}}$ and $\Delta^{36}\text{S}_{\text{CDT}}$ to anchor our data to the CDT scale, allowing direct comparison between $\Delta^{33}\text{S}$ data reported herein and those published from MORBs and OIBs (Figs. 5-9)

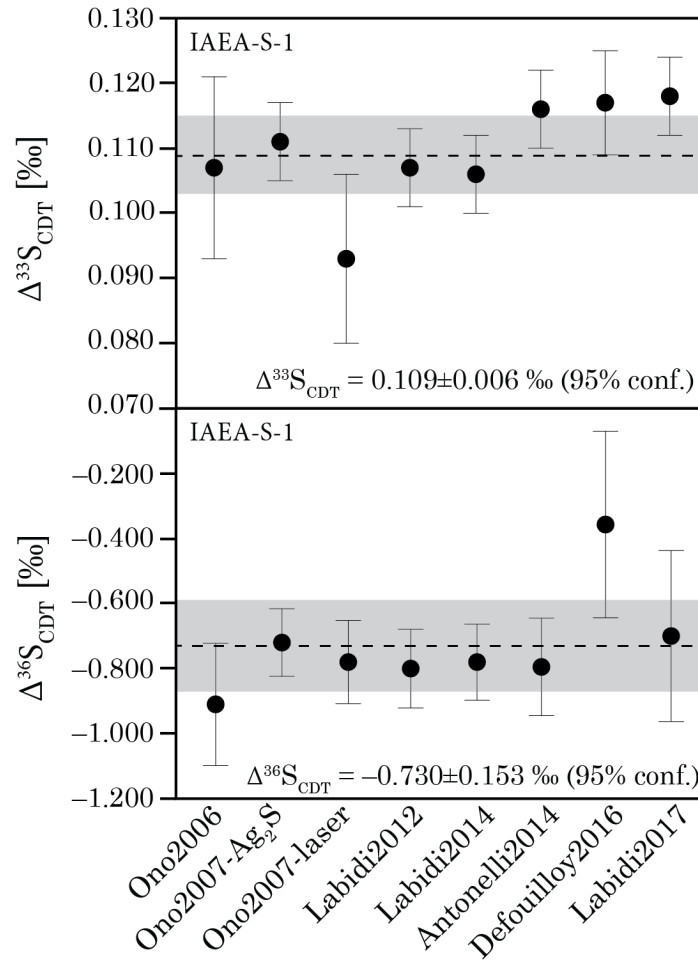


Figure S2 Published $\Delta^{33}\text{S}_{\text{CDT}}$ values of the IAEA-S-1 Ag_2S standard material. The $\Delta^{33}\text{S}_{\text{CDT}}$ value of IAEA-S-1 used to define the CDT scale for $\Delta^{33}\text{S}$. All $\Delta^{33}\text{S}_{\text{CDT}}$ values are based on measurements of IAEA-S-1 and CDT extracted as Ag_2S , except for the lowest $\Delta^{33}\text{S}_{\text{CDT}} = 0.093 \pm 0.013$ estimate, which is based on three *in situ* KBr laser fluorination analyses of CDT (Ono et al. 2007). All estimates overlap within 2σ . Error bars represent the propagated 1σ error from the IAEA-S-1 and CDT measurements reported in each study. The grey field reflects the 95% confidence interval surrounding the average value of 8 reported IAEA-S-1 versus CDT definitions (Ono et al. (2006, 2007; Labidi et al. 2012, 2014, 2017; Antonelli et al. 2014; Defouilloy et al. 2016).

2. Evaluation of magmatic S degassing

Sulfur degasses from melts dominantly as SO_2 and H_2S , with $\text{SO}_2/\text{H}_2\text{S}(\text{g})$ determined primarily by the degassing pressure (Gaillard et al. 2011). The $\text{SO}_2/\text{H}_2\text{S}$ ratio is expected to be > 1 at pressures below equivalent ~ 200 m water pressure, but H_2S is the main degassing species at higher pressures (Gaillard et al. 2011). As a result, during basaltic magma ascent to the surface during a subglacial eruption, the dominant degassing species is H_2S .

According to experimental data on S solubility, degassing of S in H_2O -poor tholeiitic basalts starts already at c. 150 MPa (~ 6 km crustal depth; Wallace and Edmonds 2011). However, relatively little degassing takes place above pressures of ~ 10 MPa (Wallace and Edmonds

2011). Therefore, high sulfur contents are preserved in subglacial pillow rim glasses if emplacement takes place under sufficient pressure, and if quenching occurs before microlite crystallization (Moore and Calk 1991). The observation that matrix glasses in subaerial lavas that were emplaced at 1 atm have relatively high sulfur contents between 300-1600 ppm (0-80% degassing relative to the initial S content; Fig 2a) implies that decompression degassing in rapidly quenched glasses is kinetically limited. Therefore, degassing estimates based on experimental S solubility limits probably overestimate the degree of degassing in subglacial glasses. In comparison, microcrystalline subaerial lavas have low bulk S concentrations (< 100 ppm; B-ALK, I-ICE and A-THO), indicating degassing of > 90 % of their primary S content.

We identify degassing in the subglacial glasses using two proxies: S vs. MgO trends (Fig. 2a) and $S^{6+}/\Sigma S$ (Fig. S3). Compiled S data from Icelandic melt inclusions define a trend of rising S concentrations in Phase 1 followed by a decreasing trend in Phase 2 (Fig. 2a). Most subglacial glasses plot subparallel to these trends (Fig. 2a), which implies that they haven't experienced significant S degassing. This is expected for basalts that erupt below an ice cover thicker than ~200-350 m, corresponding to a threshold pressure of ~2-3 MPa above which extensive S degassing is inhibited (Moore and Calk 1991). Fourteen samples that clearly deviate from the S vs. MgO trends toward lower S concentrations are interpreted to be partly degassed with respect to S (A1, A3, A6, A32, THOR-1, STORID-1, SELJA-1, SAL-601, BOTN-1, HNAUS-1, OLAF-1, NAL-460, KVK-202, KVK-205). These samples were likely erupted below a thinner ice cover. Elevated $S^{6+}/\Sigma S$ of 0.28-0.43 are observed in the low-S subglacial glasses A3, A6, NAL-460, BOTN-1, HNAUS-1 and the subaerial obsidian sample A-THO. This is interpreted to indicate eruptive degassing of a gas with high H_2S/SO_2 , as H_2S is likely to sequester dissolved S^{2-} from the melt. For sample KVK-205, $S^{6+}/\Sigma S = 0.08 \pm 0.2$ is instead lower than expected (Fig. S3), which may be the result of shallow degassing with high SO_2/H_2S .

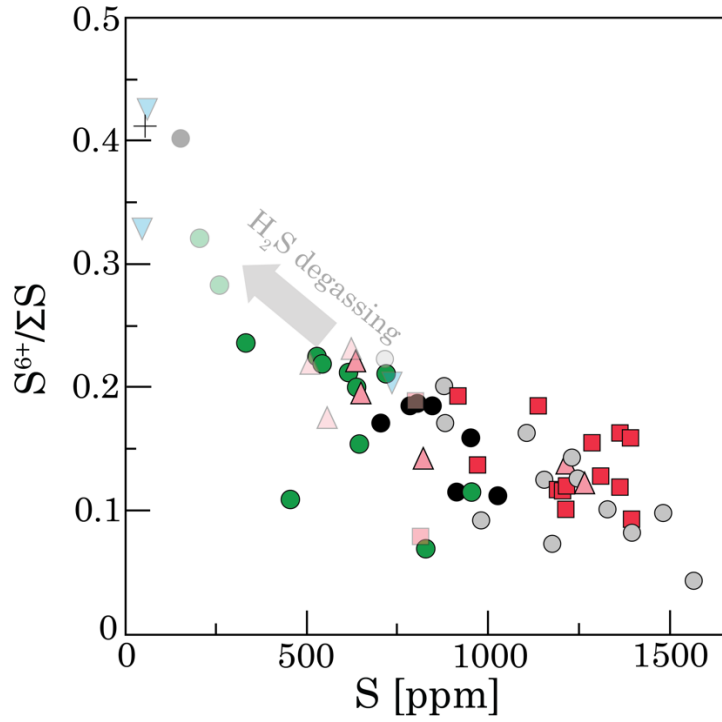


Figure S3 $S^{6+}/\Sigma S$ versus S . Elevated $S^{6+}/\Sigma S$ is a clear degassing signal seen in all low- S samples ($S < 250$ ppm). The likely explanation is eruptive degassing of gas with low SO_2/H_2S . Notably, moderately degassed samples do not have elevated $S^{6+}/\Sigma S$. Symbols as in Fig. 2. Strongly and moderately degassed samples are shown as transparent symbols.

3. Model I: Quantification of sulfide melt formation

The weight fraction X_{sulf} of the forming sulfide melt can be quantified independently using $[S]$ or $[Cu]$ (or other chalcophile elements) using the relationship

$$D_i^{\text{min-liq}} = X_{\text{sulf}} D_i^{\text{sulf-liq}} + (1 - X_{\text{sulf}}) D_i^{\text{sil-liq}} \quad \text{Eq. 5}$$

where $D_i^{\text{sulf-liq}}$ and $D_i^{\text{sil-liq}}$ are the distribution coefficients of $i = S$ or Cu between silicate minerals and melt, and sulfides and melt, respectively (c.f. Labidi et al. 2014). $D_i^{\text{min-liq}}$, the empirical bulk distribution coefficient, is calculated from concentrations of i at the beginning ($C_{i,0}$) and end ($C_{i,1}$) of a phase as

$$D_i^{\text{min-liq}} = \frac{\log(C_{i,1}/C_{i,0})}{\log F} + 1 \quad \text{Eq. 6}$$

where F is the fraction of remaining melt/crystallized minerals. Assuming fractional distillation, the Rayleigh fractionation equation can be used to estimate F :

$$F = \left(\frac{C_{j,1}}{C_{j,0}} \right)^{\frac{1}{D_j^{\text{min-liq}} - 1}} \quad \text{Eq. 7}$$

where $C_{j,1}$ and $C_{j,0}$ are the initial and final concentrations of an incompatible element and $D_j^{\text{min-liq}}$ is the bulk distribution coefficient of j . We use $j = \text{Th}$ to calculate F . Thorium is incompatible in both silicate minerals and sulfide melts as well as in Fe-Ti oxides, with a bulk distribution coefficient of $D_{\text{Th}}^{\text{min-liq}} = 0.007$ estimated for the Kverkfjöll suite (Kaikkonen 2017). Similar results for F within ± 0.05 are derived using other incompatible elements such as Ce ($D_{\text{Ce}}^{\text{min-liq}} = 0.07$) and Zr ($D_{\text{Zr}}^{\text{min-liq}} = 0.06$) (Kaikkonen 2017). X_{sulf} can be then calculated by solving Eq. 3.

A similar computation can be undertaken for concentration ratios of elements j and i , that change with fractional crystallization according to

$$\frac{C_{i,1}}{C_{j,1}} = \frac{C_{i,0}}{C_{j,0}} F^{(D_i^{\text{min-liq}} - D_j^{\text{min-liq}})} \quad \text{Eq. 8}$$

If $D_i^{\text{sil-liq}} = D_j^{\text{sil-liq}}$ and $D_j^{\text{sulf-liq}} \approx 0$, Eq. 8 can be rewritten as

$$\frac{C_{i,1}}{C_{j,1}} = \frac{C_{i,0}}{C_{j,0}} F^{(D_i^{\text{sulf-liq}} - D_j^{\text{sil-liq}})} \quad \text{Eq. 9}$$

Eq. 3 can then be used to determine X_{sulf} using element pairs such as Cu/Y (Labidi et al. 2015)

4. Bulk $\delta^{34}\text{S}$ value of Icelandic melts

Assuming isotopic equilibrium between dissolved sulfide and sulfate in undegassed melts and extrapolating the experimental results of Miyoshi et al. (1984) to 1250 °C using their Eq (3), we use a fractionation factor of

$$\Delta^{34}\text{S}_{\text{sulfate-sulfide}} = \delta^{34}\text{S}_{\text{sulfate}} - \delta^{34}\text{S}_{\text{sulfide}} = 7.4 \times 10^6 / T^2 - 0.19 \quad \text{Eq. 10}$$

where T is temperature in K. Eq. 10 gives $\Delta^{34}\text{S}_{\text{sulfate-sulfide}} \approx +3 \text{ ‰}$ for $T = 1250 \text{ °C}$. If all the sulfur in the melt is dissolved as S^{6+} and S^{2-} , we can state that

$$\delta^{34}\text{S}_{\Sigma\text{S}} = f_{\text{sulfate}} \times \delta^{34}\text{S}_{\text{sulfate}} + (1 - f_{\text{sulfate}}) \times \delta^{34}\text{S}_{\text{sulfide}} \quad \text{Eq. 11}$$

where $f_{\text{sulfate}} = \text{S}^{6+}/\Sigma\text{S}$. Combining Eqs. 10 and 11, we can estimate $\delta^{34}\text{S}_{\Sigma\text{S}}$ using

$$\delta^{34}\text{S}_{\Sigma\text{S}} = f_{\text{sulfate}} \times \Delta^{34}\text{S}_{\text{sulfate-sulfide}} + \delta^{34}\text{S}_{\text{sulfide}} \quad \text{Eq. 12}$$

The size of the correction term $f_{\text{sulfate}} \times \Delta^{34}\text{S}_{\text{sulfate-sulfide}}$ varies with $\text{S}^{6+}/\Sigma\text{S}$ and T. Based on our $\Delta\text{S}_{\text{K}\alpha}$ measurements, we estimate to a $\delta^{34}\text{S}_{\Sigma\text{S}}$ value that is between 0.1 and 0.7‰ more positive than the measured $\delta^{34}\text{S}_{\text{S}^{2-}}$ values (Table S-2). Notably, in the case of the highly oxidized rhyolite sample A-THO ($x = 0.41$), with an estimated equilibrium $T = 950 \text{ °C}$ (c.f. Schattel et al. 2014), the measured $\delta^{34}\text{S}_{\text{S}^{2-}}$ value of +3.80‰ requires a correction of c. +1.95‰ to a $\delta^{34}\text{S}_{\Sigma\text{S}}$ value of +5.75 ‰. The uncorrected value is more similar to the A-THO value of 4.2 ‰ measured by Thorssander (1989) using the Kiba extraction method, which doesn't separate between the sulfur species. This poses the question whether sulfur species in degassed rhyolitic melts attain isotopic equilibrium, although a thorough assessment is outside the scope of this paper. A deviation from equilibrium $\Delta^{34}\text{S}_{\text{sulfate-sulfide}}$ values toward more positive values measured in Samoan and Hawaiian basalts have been attributed to kinetic fractionation during shallow sulfur degassing, which favors partitioning of the $^{32}\text{SO}_2$ ions to the vapor phase (Sakai et al. 1982; Labidi et al. 2015) from the sulfate fraction of the melt. The implication is that SO_2 degassing takes place rapidly at shallow depths and does not impose fractionation on the measured $\delta^{34}\text{S}_{\text{sulfide}}$ values (Labidi et al. 2015). However, isotopic equilibrium between S species is more likely to be attained in undegassed melts during their considerably longer residence time in high-T magmatic reservoirs

5. Model II: $\delta^{34}\text{S}$ fractionation during degassing

S isotope fractionation during degassing can be modelled by estimating a bulk $a_{\text{gas-melt}}$ fractionation constant, defined by

$$\varepsilon^{34}\text{S}_{\text{gas-melt}} = \delta^{34}\text{S}_{\text{gas}} - \delta^{34}\text{S}_{\text{melt}} \approx 1000 \ln a_{\text{gas-melt}} \quad \text{Eq. 13}$$

Following Mandeville et al. (2009), we estimate $1000 \ln a_{\text{gas-melt}}$ by assuming isotopic equilibrium between the main S species in the gas (SO_2 and H_2S) and melt (S^{6+} and S^{2-}). Then,

$$1000 \ln a_{\text{gas-melt}} = f_{\text{SO}_2} \times f_{\text{S}^{6+}} \times 1000 \ln a_{\text{SO}_2-\text{S}^{6+}} + f_{\text{SO}_2} \times (1 - f_{\text{S}^{6+}}) \times 1000 \ln a_{\text{SO}_2-\text{S}^{2-}} + (1 - f_{\text{SO}_2}) \times f_{\text{S}^{6+}} \times 1000 \ln a_{\text{H}_2\text{S}-\text{S}^{6+}} + (1 - f_{\text{SO}_2})(1 - f_{\text{S}^{6+}}) 1000 \ln a_{\text{H}_2\text{S}-\text{S}^{2-}} \quad \text{Eq. 14}$$

where $f_{\text{SO}_2} = \text{SO}_2 / (\text{SO}_2 + \text{H}_2\text{S})$ of the gas phase and $f_{\text{S}^{6+}} = \text{S}^{6+} / (\text{S}^{6+} + \text{S}^{2-})$ of the melt. Equilibrium fractionation factors for the pairs $\text{SO}_2(\text{g})\text{-H}_2\text{S}(\text{g})$, $\text{H}_2\text{S}(\text{g})\text{-S}^{2-}(\text{m})$, $\text{S}^{6+}(\text{m})\text{-H}_2\text{S}(\text{g})$ and $\text{S}^{6+}(\text{m})\text{-S}^{2-}(\text{m})$ have been determined experimentally as

$$1000 \ln a_{\text{SO}_2-\text{H}_2\text{S}} = -0.42 \times \frac{10^9}{T^3} + 4.367 \times \frac{10^6}{T^2} - 0.105 \times \frac{10^3}{T} - 0.41 \quad (\text{Taylor 1986}) \quad \text{Eq. 15}$$

$$1000 \ln a_{\text{H}_2\text{S}-\text{S}^{2-}} = 1.1 \times \frac{10^6}{T^2} - 0.19 \quad (\text{Taylor 1986}) \quad \text{Eq. 16}$$

$$1000 \ln a_{\text{S}^{6+}-\text{S}^{2-}} = 7.4 \times \frac{10^6}{T^2} - 0.19 \quad (\text{Miyoshi et al. 1984}) \quad \text{Eq. 17}$$

$$1000 \ln a_{\text{S}^{6+}-\text{H}_2\text{S}} = 6.5 \times \frac{10^6}{T^2} \quad (\text{Miyoshi et al. 1984}) \quad \text{Eq. 18}$$

The fractionation factors for the pairs $\text{SO}_2(\text{g})\text{-S}^{6+}(\text{m})$ and $\text{SO}_2(\text{g})\text{-S}^{2-}(\text{m})$ can be expressed as

$$1000 \ln a_{\text{SO}_2-\text{S}^{6+}} = 1000 \ln a_{\text{SO}_2-\text{H}_2\text{S}} - 1000 \ln a_{\text{S}^{6+}-\text{H}_2\text{S}} \quad \text{Eq. 19}$$

$$1000 \ln a_{\text{SO}_2-\text{S}^{2-}} = 1000 \ln a_{\text{SO}_2-\text{S}^{6+}} + 1000 \ln a_{\text{S}^{6+}-\text{S}^{2-}} \quad \text{Eq. 20}$$

For reference, the fractionation constants calculated with Eqs. 15-20 are $a_{\text{SO}_2-\text{S}^{6+}} \approx 0.9984$, $a_{\text{SO}_2-\text{S}^{2-}} \approx 1.0016$, $a_{\text{H}_2\text{S}-\text{S}^{6+}} \approx 0.9970$ and $a_{\text{H}_2\text{S}-\text{S}^{2-}} \approx 1.0003$ at $T = 1200^\circ\text{C}$, and $a_{\text{SO}_2-\text{S}^{6+}} \approx 0.9973$, $a_{\text{SO}_2-\text{S}^{2-}} \approx 1.0035$, $a_{\text{H}_2\text{S}-\text{S}^{6+}} \approx 0.9944$ and $a_{\text{H}_2\text{S}-\text{S}^{2-}} \approx 1.00076$ at $T = 800^\circ\text{C}$. The largest fractionation is seen for degassing of $\text{H}_2\text{S}(\text{g})$ from the $\text{S}^{6+}(\text{m})$ pool, because of the large difference in S oxidation state from 6+ to 2- (Marini et al. 2011). For the same reason, the redox-neutral degassing of $\text{H}_2\text{S}(\text{g})$ from the $\text{S}^{2-}(\text{m})$ pool is only associated with minor $\delta^{34}\text{S}$ fractionation and the associated term in Eq (16) is frequently ignored (Mandeville et al. 2009, Marini et al. 2011).

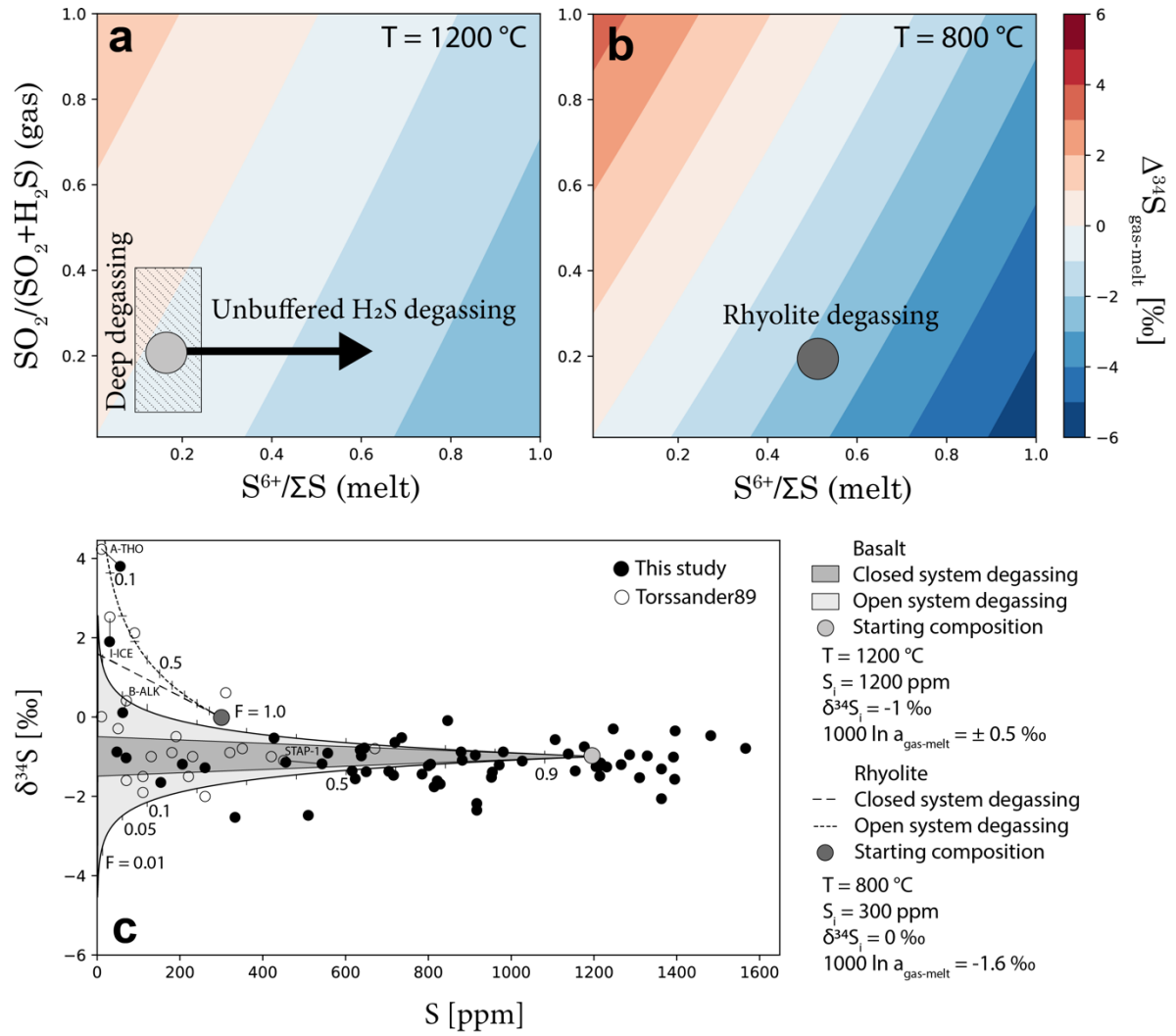


Figure S4 Effect of S speciation of gas and melt on $\Delta^{34}\text{S}_{\text{gas-melt}}$ fractionation at (a) 1200 °C and (b) 800 °C. (c) Open- and closed-system degassing models for basalts and rhyolites. A starting value of $S_i = 300$ ppm was used for the rhyolite model, as S concentrations in rhyolitic melt inclusions rarely exceed 300 ppm in Iceland.

6. Relationship between melt $S^{6+}/\Sigma S$ and oxygen fugacity

Buffering of melt $S^{6+}/\Sigma S$ may occur through electron-exchange equilibrium with either dissolved Fe or H_2O (Métrich et al. 2009, Jugo et al. 2010, Nash et al. 2019). Experimental data of Nash et al. (2019) supports the redox coupling between Fe and S according to Eq. (4). This buffer reaction hinders an unchecked increase in the $S^{6+}/\Sigma S$ of the melt during sequestration of S^{2-} by a sulfide melt. Instead, the resulting increase in oxidation potential of the melt is accommodated by an increasing $\text{Fe}^{3+}/\text{Fe}^{2+}$ according to the empirical linear relationship between $\log(S^{6+}/\text{S}^{2-})$ and $\log(\text{Fe}^{3+}/\text{Fe}^{2+})$ reported in Eq. (11) of Nash et al. (2019):

$$\log \frac{S^{6+}}{S^{2-}} = 8 \log \frac{Fe^{3+}}{Fe^{2+}} + \frac{8.743 \times 10^6}{T^2} - \frac{27703}{T} \quad \text{Eq. 21}$$

An almost complete turnover from $S^{6+}/\Sigma S \approx 0$ to $S^{6+}/\Sigma S \approx 1$ takes place over a relatively narrow interval of $Fe^{3+}/\Sigma Fe$ values (between 0.1 and 0.3 at 1200 °C; Fig. S5a), approximately equivalent to a change from $\Delta FMQ = 0$ to +1. The T dependence Eq. (21) means that at constant $Fe^{3+}/\Sigma Fe$, hotter melts have higher $S^{6+}/\Sigma S$ (Fig. S5b). Icelandic basalts are hotter (Matthews et al. 2016) and more oxidized than MORBs, which explains why $S^{6+}/\Sigma S$ measured in our study are higher than reported $S^{6+}/\Sigma S$ values of MORB glasses (< 0.1) (Fig. 2b).

Notably, the T dependence of Eq. 21 may further explain the somewhat counterintuitive observation that $S^{6+}/\Sigma S$ of Icelandic melts decrease during magma evolution from MgO = 10 to 6 wt.% (Fig. 2b), while simultaneously, Fe^{3+}/Fe^{2+} stay roughly constant or increase because of preferential Fe^{2+} sequestration by olivine ($D_{Ol}^{Fe_2O_3} < 0.1$) and clinopyroxene ($D_{cpx}^{Fe_2O_3} = 0.45$) (Mallmann and O'Neill 2009, Shorttle et al. 2015).

Figure S5 illustrates different scenarios for how $S^{6+}/\Sigma S$ is expected to vary during magma evolution and associated changes in $Fe^{3+}/\Sigma Fe$ and T. The modeled decrease in $S^{6+}/\Sigma S$ during magma evolution closely matches the Icelandic data and shows that melt $S^{6+}/\Sigma S$ is mainly controlled by melt T above MgO = 6 wt.% (Fig. 2b). Below 6 wt.% MgO, sequestration of S^{2-} by immiscible sulfide melts becomes the dominant control on $S^{6+}/\Sigma S$, leading to a reversal of the $S^{6+}/\Sigma S$ vs. MgO trend (Fig. 2b, Fig. S6).

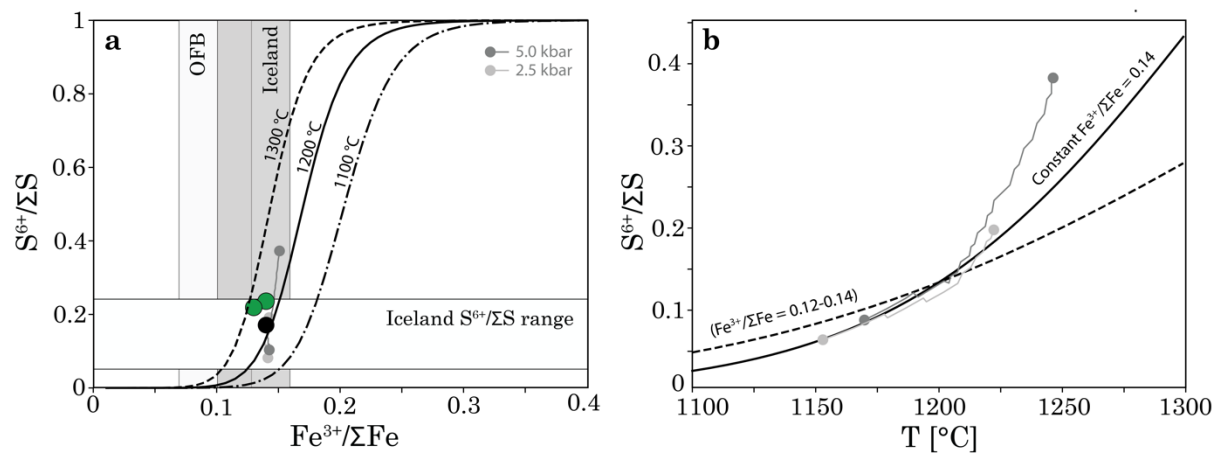


Figure S5 Relationship between $S^{6+}/\Sigma S$, $Fe^{3+}/\Sigma Fe$ and temperature. **(a)** S-Fe buffer (Eq. 4) curves are shown for T = 1100, 1200 and 1300 °C, calculated using Eq. (15). 95% of published $Fe^{3+}/\Sigma Fe$ values for ocean floor basalts (OFBs) fall within the light gray shaded field (O'Neill 2020). Published range of $Fe^{3+}/\Sigma Fe$ for Icelandic and Reykjanes Ridge pillow rim glasses (Óskarsson et al. 1994, Novella et al. 2020) is more oxidized (dark gray field). Coupled data for samples MID-1, STAP-1 and NAL-263

are shown (this study, Óskarsson et al. 1994). **(b)** The temperature dependence of $S^{6+}/\Sigma S$ is calculated using Eq. (15). Solid curve shows the solution for constant $Fe^{3+}/\Sigma Fe = 0.14$ scenario. Dashed line shows a hypothetical scenario with linearly increasing $Fe^{3+}/\Sigma Fe$ from 0.10 at $T = 1300$ °C to 0.12 at $T = 1100$ °C, showing that S can become reduced even during moderate oxidation of Fe. In (a) and (b), the effect of fractional crystallization on $S^{6+}/\Sigma S$ is modelled with COMAGMAT v3.72 (Aroskin et al. 2018) using sample NAL-688 as starting composition, buffered at FMQ+0.2 in isobaric conditions at 2.5 kbar (light grey circle-ended line) and 5 kbar (dark grey circle-ended line) to MgO = 6 wt.%. The controlling factor on $S^{6+}/\Sigma S$ is the drop in liquidus temperature of 69-80 °C accompanying fractional crystallization from 9.8 to 6.0 wt. MgO, that has a net effect of $\Delta S^{6+}/\Sigma S = -0.14$ and -0.30 at 2.5 and 5 kbar, respectively. Although limited, the three data points in (a) seem compatible with the modelled FC curves.

7. Model III: Effect of sulfide fractionation on $\delta^{34}S$

In MORBs, sulfide melt fractionation only has a tangential effect on the $\delta^{34}S_{S^{2-}}$ values because virtually all sulfur is dissolved as S^{2-} (Labidi et al. 2014). This is not necessarily case for more oxidized melts, if the $S^{6+}/\Sigma S$ is buffered (Labidi et al. 2015). The effects of sulfide fractionation and $S^{6+}/\Sigma S$ buffering on melt $\delta^{34}S_{\Sigma S}$ and $\delta^{34}S_{S^{2-}}$ values can be quantified separately for non-buffered (7.1) and buffered (7.2) scenarios (Fig. S6).

7.1 Non-buffered system

The initial $S^{6+}/\Sigma S$ ratio of the melt is defined as

$$X_0 = [S^{6+}/\Sigma S]_0 = \frac{S_0^{6+}}{S_0^{2-} + S_0^{6+}} \quad \text{Eq. 22}$$

If $\delta^{34}S_0^{6+}$ and $\delta^{34}S_0^{2-}$ denote the initial $\delta^{34}S$ values of the sulfate and sulfide pools, respectively, the initial bulk $\delta^{34}S$ value is

$$\delta^{34}S_0^{\text{bulk}} = X_0 \times \delta^{34}S_0^{6+} + (1 - X_0) \times \delta^{34}S_0^{2-} \quad \text{Eq. 23}$$

Assuming that the sulfide melt only taps the S^{2-} pool of the silicate melt, sulfide fractionation in a non-buffered system leads to an increase in $S^{6+}/\Sigma S$, so that

$$X_1 = [S^{6+}/\Sigma S]_1 = \frac{S_0^{6+}}{S_0^{2-} - x_{\text{sulf}} + S_0^{6+}} \quad \text{Eq. 24}$$

where x_{sulf} is the weight fraction of S^{2-} sequestered by sulfide melt. Because $\Delta^{34}S_{sulfide-S^{2-}(m)} \approx 0$, the isotopic values of the sulfate and sulfide pools in the silicate melt remain the same, so that

$$\delta^{34}S_0^{6+} = \delta^{34}S_1^{6+} \quad \text{Eq. 25}$$

$$\delta^{34}S_0^{2-} = \delta^{34}S_1^{2-} \quad \text{Eq. 26}$$

However, the bulk $\delta^{34}S$ value

$$\begin{aligned} \delta^{34}S_1^{bulk} &= X_1 \times \delta^{34}S_1^{6+} + (1 - X_1) \times \delta^{34}S_1^{2-} = \\ &= X_1 \times \delta^{34}S_0^{6+} + (1 - X_1) \times \delta^{34}S_0^{2-} \end{aligned} \quad \text{Eq. 27}$$

will increase because the proportion of isotopically heavier S^{6+} increases.

7.2 Redox buffered system

In a system where the $S^{6+}/\Sigma S$ is buffered, subsequent conversion of S^{6+} to S^{2-} by some amount will take place, so that

$$S_2^{2-} = S_0^{2-} - x_{sulf} + a \quad \text{Eq. 28}$$

$$S_2^{6+} = S_0^{6+} - a \quad \text{Eq. 29}$$

$$X_2 = \frac{S_0^{6+} - a}{S_0^{2-} - x_{sulf} + S_0^{6+}} \quad \text{Eq. 30}$$

The conversion of S^{6+} to S^{2-} will not change the bulk $\delta^{34}S$ value, so that

$$\delta^{34}S_2^{bulk} = X_2 \times \delta^{34}S_2^{6+} + (1 - X_2) \times \delta^{34}S_2^{2-} = \delta^{34}S_1^{bulk} \quad \text{Eq. 31}$$

However, buffering will impose a change on $\delta^{34}S^{6+}$ and $\delta^{34}S^{2-}$. For an end-member scenario where $S^{6+}/\Sigma S$ is buffered to its original value, i.e., $X_0 = X_2$, assuming isotopic equilibrium between S^{2-} and S^{6+} and combining Eqs. 13, 25, 26 and 31, we can state that

$$\begin{cases} X_0 \times \delta^{34}S_2^{6+} + (1 - X_0) \times \delta^{34}S_2^{2-} = X_1 \times \delta^{34}S_0^{6+} + (1 - X_1) \times \delta^{34}S_0^{2-} \\ \delta^{34}S_2^{6+} = \delta^{34}S_2^{2-} + \epsilon^{34}S_{S^{6+}-S^{2-}} \end{cases} \quad \text{Eq. 32}$$

We can then solve for $\delta^{34}S_2^{6+}$ and $\delta^{34}S_2^{2-}$ to get

$$\delta^{34}S_2^{6+} = X_1 \times \delta^{34}S_0^{6+} + (1 - X_1) \times \delta^{34}S_0^{2-} + \epsilon^{34}S_{S^{6+}-S^{2-}} \times (1 - X_0) \quad \text{Eq. 33}$$

$$\delta^{34}S_2^{2-} = X_1 \times \delta^{34}S_0^{6+} + (1 - X_1) \times \delta^{34}S_0^{2-} - \epsilon^{34}S_{S^{6+}-S^{2-}} \times X_0 \quad \text{Eq. 34}$$

Alternatively, we note that with the given assumptions, the change Δ^{34} in $\delta^{34}S$ is the same for both $\delta^{34}S_{S^{2-}}$, $\delta^{34}S_{S^{6+}}$ and $\delta^{34}S_{\Sigma S}$ (Fig. S6c) so that

$$\Delta_1^{34} = \Delta_2^{34} = \delta^{34}S_1^{\text{bulk}} - \delta^{34}S_0^{\text{bulk}} = (X_1 - X_0) \times \epsilon^{34}S_{S^{6+}-S^{2-}} \quad \text{Eq. 35}$$

which yields the expressions

$$\delta^{34}S_2^{6+} = \delta^{34}S_0^{6+} + \Delta_1^{34} \quad \text{Eq. 36}$$

$$\delta^{34}S_2^{2-} = \delta^{34}S_0^{2-} + \Delta_1^{34} \quad \text{Eq. 37}$$

that are equivalent to Eqs. 33 and 34. For this scenario, the amount of converted sulfur a can be expressed as

$$a = S_0^{6+} - X_0(S_0^{2-} - x_{\text{sulf}} + S_0^{6+}) \quad \text{Eq. 38}$$

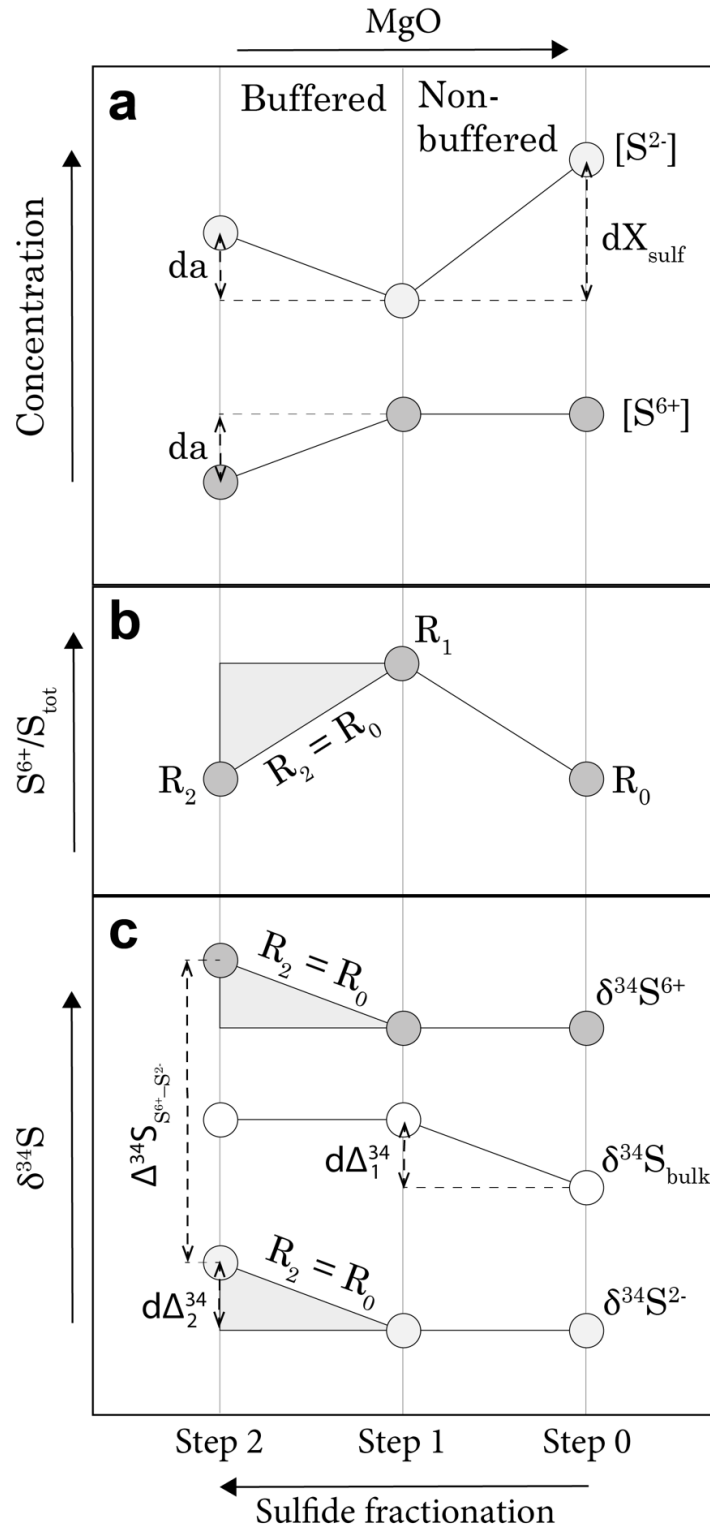


Figure S6 Schematic representation of the effects of sulfide fractionation on melt **(a)** S^{2-} and S^{6+} concentrations, **(b)** $S^{6+}/\Sigma S$, and **(c)** $\delta^{34}S$. Step 0 shows the initial state, step 1 after sulfide fractionation with no redox buffering, and step 2 after redox buffering. The magnitude of da , the amount of S^{6+} to S^{2-} conversion, depends on the redox buffer, and can assume values between 0 (no buffering) and da_{max} , which occurs when $S^{6+}/\Sigma S$ is fully buffered so that $R_2 = R_0$. This condition limits the maximum effect of sulfide fractionation on $\delta^{34}S_{S^{2-}}$ and $\delta^{34}S_{S^{6+}}$ so that $\Delta_{2,max}^{34} = \Delta_1^{34}$.

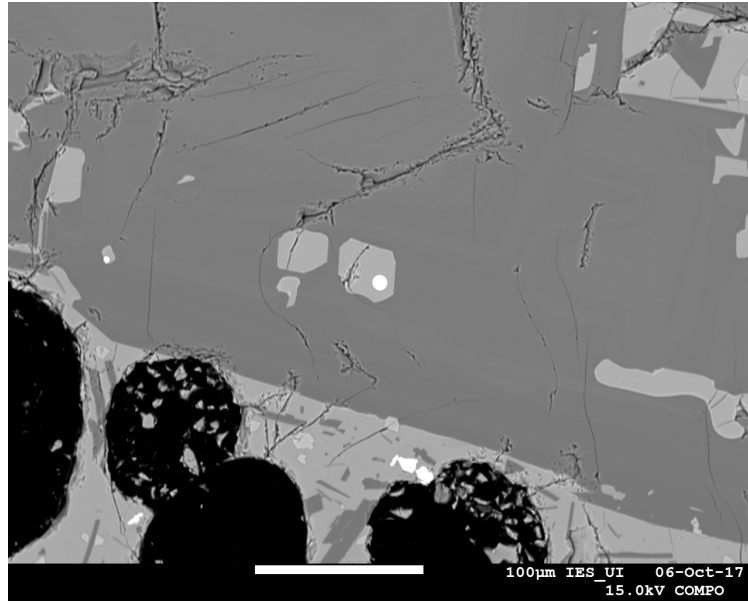


Figure S7 Sulfide globules (bright) in plagioclase-hosted melt inclusions in a Kverkfjöll scoria sample (KVK-212). This sample was not analyzed in this study.

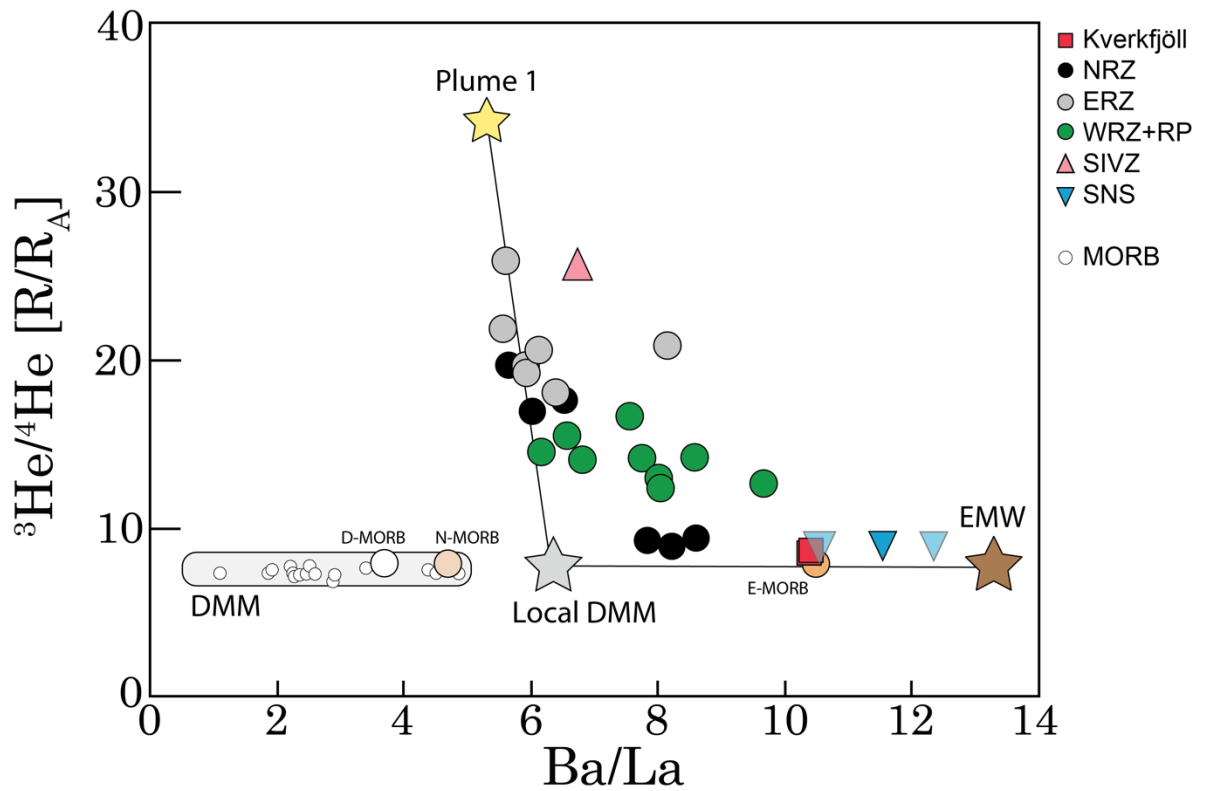


Figure S8 $^3\text{He}/^4\text{He}$ versus Ba/La. Subduction fluids have elevated Ba/La compared to DMM. We thus assume that the enriched mantle wedge component (EMW) has a high Ba/La (~ 13.5). Highest Ba/La in Iceland are observed in the Kverkfjöll and Snæfellsnes samples that both have MORB-like $^3\text{He}/^4\text{He}$. Kverkfjöll plots close to the estimated composition of E-MORB (Gale et al. 2013). The $^3\text{He}/^4\text{He}$ vs. Ba/La systematics are compatible with the subduction fluid origin of low $\delta^{34}\text{S}$ and $\Delta^{33}\text{S}$ signatures in the Icelandic mantle (Fig. 8).

Supplementary references

- Antonelli, M. A., Kim, S. T., Peters, M., Labidi, J., Cartigny, P., Walker, R. J., Lyons, J.R., Hoek, J., & Farquhar, J. (2014). Early inner solar system origin for anomalous sulfur isotopes in differentiated protoplanets. *Proceedings of the National Academy of Sciences*, 111(50), 17749-17754.
- Bali, E., Hartley, M. E., Halldórsson, S. A., Gudfinnsson, G. H., & Jakobsson, S. (2018). Melt inclusion constraints on volatile systematics and degassing history of the 2014–2015 Holuhraun eruption, Iceland. *Contributions to Mineralogy and Petrology*, 173(2), 1-21.
- Carroll M. R. and Rutherford M. J. (1988) Sulfur speciation in hydrous experimental glasses of varying oxidation state: results from measured wavelength shifts of sulfur X-rays. *Am. Mineral.* 73, 845–849.
- Defouilloy, C., Cartigny, P., Assayag, N., Moynier, F., & Barrat, J. A. (2016). High-precision sulfur isotope composition of enstatite meteorites and implications of the formation and evolution of their parent bodies. *Geochimica et Cosmochimica Acta*, 172, 393-409.
- Gaillard, F., Scaillet, B., & Arndt, N. T. (2011). Atmospheric oxygenation caused by a change in volcanic degassing pressure. *Nature*, 478(7368), 229-232.
- Gale, A., Dalton, C. A., Langmuir, C. H., Su, Y., & Schilling, J. G. (2013). The mean composition of ocean ridge basalts. *Geochemistry, Geophysics, Geosystems*, 14(3), 489-518.
- Guillong M, Meier D.L, Allan M.M, Heinrich C.A., & Yardley B.W. (2008) SILLS: a MATLAB-based program for the reduction of laser ablation ICP–MS data of homogeneous materials and inclusions. *Mineralogical Association of Canada Short Course*, v. 40, 328–333
- Hauri, E. H., J. Wang, J. E. Dixon, P. L. King, C. Mandeville, & S. Newman. 2002. SIMS Investigations of volatiles in silicate glasses, 1: Calibration, matrix effects and comparisons with FTIR. *Chemical Geology*, 183, 99-114.
- Kaikkonen, R. MSc Thesis (2017). Oulu School of Mining.
- Labidi, J., Farquhar, J., Alexander, C. O. D., Eldridge, D. L., & Oduro, H. (2017). Mass independent sulfur isotope signatures in CMs: Implications for sulfur chemistry in the early solar system. *Geochimica et Cosmochimica Acta*, 196, 326-350.
- Mallmann, G., & O'Neill, H. S. C. (2009). The crystal/melt partitioning of V during mantle melting as a function of oxygen fugacity compared with some other elements (Al, P, Ca, Sc, Ti, Cr, Fe, Ga, Y, Zr and Nb). *Journal of Petrology*, 50(9), 1765-1794.
- Mandeville, C. W., Webster, J. D., Tappen, C., Taylor, B. E., Timbal, A., Sasaki, A., Hauri, E., & Bacon, C. R. (2009). Stable isotope and petrologic evidence for open-system degassing during the climactic and pre-climactic eruptions of Mt. Mazama, Crater Lake, Oregon. *Geochimica et Cosmochimica Acta*, 73(10), 2978-3012.
- Marini, L., Moretti, R., & Accornero, M. (2011) Sulfur isotopes in magmatic-hydrothermal systems, melts, and magmas. *Reviews in Mineralogy and Geochemistry*, 73, 423–492.
- Matthews, S., Shorttle, O., & MacLennan, J. (2016). The temperature of the Icelandic mantle from olivine-spinel aluminum exchange thermometry. *Geochemistry, Geophysics, Geosystems*, 17(11), 4725-4752.
- Métrich N., Berry A. J., O'Neill H. St. C., & Susini J. (2009) The oxidation state of sulfur in synthetic and natural glasses determined by X-ray absorption spectroscopy. *Geochimica et Cosmochimica Acta*, 73, 2382–2399.
- Miyoshi, T., Sakai, H., & Chiba, H. (1984). Experimental study of sulfur isotope fractionation factors between sulfate and sulfide in high temperature melts. *Geochemical Journal*, 18(2), 75-84.
- Moilanen, M., Hanski, E., Konnunaho, J., Törmänen, T., Yang, S.H., Lahaye, Y., O'Brien, H., & Illikainen, J., 2020, Composition of iron oxides in Archean and Paleoproterozoic mafic-ultramafic hosted Ni-Cu-PGE deposits in northern Fennoscandia: application to mineral exploration: *Mineralium Deposita*, 55(8). 1515–1534.
- Moore, J. G., & Calk, L. C. (1991). Degassing and differentiation in subglacial volcanoes, Iceland. *Journal of Volcanology and Geothermal Research*, 46(1-2), 157-180.
- Nash, W. M., Smythe, D. J., & Wood, B. J. (2019). Compositional and temperature effects on sulfur speciation and solubility in silicate melts. *Earth and Planetary Science Letters*, 507, 187-198.
- Newman, S., & Lowenstern, J. B. (2002). VolatileCalc: a silicate melt–H₂O–CO₂ solution model written in Visual Basic for excel. *Computers & Geosciences*, 28(5), 597-604.
- O'Neill, H. St.C. (in press). The thermodynamic controls on sulfide saturation in silicate melts with application to Ocean Floor Basalts. AGU Geophysical Monograph, Redox variables and mechanisms in magmatism and volcanism. Editors R. Moretti and D. R. Neuville, John Wiley and Sons.
- Ono, S., Shanks III, W. C., Rouxel, O. J., & Rumble, D. (2007). S-33 constraints on the seawater sulfate contribution in modern seafloor hydrothermal vent sulfides. *Geochimica et Cosmochimica Acta*, 71(5), 1170-1182.

- Óskarsson, N., Helgason, Ö., & Steinthórsson, S. (1994). Oxidation state of iron in mantle-derived magmas of the Icelandic rift zone. *Hyperfine Interactions*, 91(1), 733-737.
- Sakai, H., Casadevall, T. J., & Moore, J. G. (1982). Chemistry and isotope ratios of sulfur in basalts and volcanic gases at Kilauea Volcano, Hawaii. *Geochimica et Cosmochimica Acta*, 46(5), 729-738.
- Schattel, N., Portnyagin, M., Golowin, R., Hoernle, K., & Bindeman, I. (2014). Contrasting conditions of rift and off-rift silicic magma origin on Iceland. *Geophysical Research Letters*, 41(16), 5813-5820.
- Taylor Jr, H. P. (1986). Igneous rocks: I. Process of isotopic fractionation and isotope systematics. Stable isotopes in high temperature geological processes. *Reviews in Mineralogy and Geochemistry*, 16, pp. 185-225